

Main Manuscript for

Improved Atmospheric Constraints on Southern Ocean CO2 Exchange

5 Yuming Jin¹, Ralph F. Keeling¹, Britton B. Stephens², Matthew C. Long², Prabir K. Patra³, Christian Rödenbeck⁴, Eric J. Morgan¹, Eric A. Kort⁵, Colm Sweeney⁶

¹Scripps Institution of Oceanography, University of California, San Diego, La Jolla, California, USA

²National Center for Atmospheric Research, Boulder, Colorado, USA

³Research Institute for Global Change, Japan Agency for Marine-Earth Science and Technology, Yokohama, 236 10 0001, Japan

⁴Max Planck Institute for Biogeochemistry, Jena, Germany

⁵Department of Atmospheric, Oceanic and Space Sciences, University of Michigan, Ann Arbor, Michigan, USA

⁶National Oceanic and Atmospheric Administration, Earth System Research Laboratory, Boulder, Colorado, USA

15 Corresponding Author: Yuming Jin

Email: y2jin@ucsd.edu

20

Author Contributions: Y.J., R.F.K., B.B.S., and M.C.L. designed the research; Y.J. performed the research; Y.J. analyzed the data; B.B.S. and E.J.M. provided aircraft CO₂ measurements from the AO2 instrument; P.K.P. provided the MIROC-ACTM CO₂ inversion products and provided discussions of bias in models; C.R. provided the Jena CarboScope CO₂ inversion product; E.J.M. supported CO₂ measurements at SIO; E.A.K. provided aircraft CO₂ measurements from the QCLS instrument; C.S. provided aircraft CO₂ measurements from the NOAA Picarro instrument and NOAA PFP sampler; Y.J., R.F.K., and B.B.S. wrote the paper; All co-authors revised the paper and provided comments; The paper also build upon a previous work of M.C.L.

Competing Interest Statement: The authors declare no competing interest.

25 Classification: Physical Sciences - Earth, Atmospheric, and Planetary Sciences

Keywords: Carbon Sink, Atmospheric Diabatic Mixing, Inverse Model, Atmospheric Transport Model, Airborne Observation

This PDF file includes:

30 Main Text Figures 1 to 5

Abstract

35

40

45

50

55

60

We present improved estimates of air-sea CO_2 exchange over three latitude bands of the Southern Ocean (SO) using atmospheric CO_2 measurements from global airborne campaigns and an atmospheric 4-box inverse model based on a mass-indexed isentropic coordinate ($M_{\theta e}$). These flux estimates show two features not clearly resolved in previous estimates based on inverting surface CO_2 measurements: a weak winter-time outgassing in the polar region, and a sharp phase transition of the seasonal flux cycles between polar/subpolar and subtropical regions. The estimates suggest much stronger summer-time uptake in the polar/subpolar regions than estimated derived from neural-network interpolation of p CO_2 from profiling floats, but somewhat weaker uptake than a recent study by Long et al (1), who used the same airborne data and multiple atmospheric transport models (ATMs) to constrain surface fluxes. Our study also uses moist static energy (MSE) budgets from reanalyses to show that most ATMs tend to have excessive diabatic mixing (transport across moist isentrope, θ_e , or $M_{\theta e}$ surfaces) at high southern latitudes in the austral summer, which leads to biases in estimates of air-sea CO_2 exchange. Furthermore, we show that the MSE-based constraint is consistent with an independent constraint on atmospheric mixing based on combining airborne and surface CO_2 observations.

Significance Statement

Precise estimates of Southern Ocean CO₂ uptake are lacking due to sparse surface-ocean observations. This study presents an alternate approach applying airborne CO₂ observations to constrain the SO air-sea CO₂ flux using a multi-box atmospheric model aligned with moist isentropes. This study improves upon prior studies that estimate flux based on atmospheric CO₂ measurements by using better-constrained estimates of atmospheric diabatic transport (transport across moist isentropes). It also allows fluxes to be resolved in finer latitude bands, thus facilitating a closer comparison with surface ocean pCO₂ observations and identifying CO₂ flux components driven by marine photosynthesis, ventilation, and warming/cooling. Our study underscores the value of aircraft measurements for precisely quantifying long-term changes in CO₂ uptake by the SO.

Introduction

Precise assessments of the air-sea CO₂ flux of the Southern Ocean (SO), which includes both natural and anthropogenic components, are of critical importance to understanding the global

carbon cycle and predicting future oceanic carbon uptake under climate change (2–5). The high-latitude SO (<58°S) was likely a significant natural source of CO₂ to the atmosphere in the preindustrial era, but has switched to being a net sink in the present-day (6). Available estimates suggest that uptake over the entire SO (<35°S) strengthened from 1980 to 2015, with significant decadal variability (5, 7–13).

Observation-based flux estimates of the entire SO remain highly uncertain. The net SO CO₂ flux has been quantified using pCO₂ measurements from ship-based and Argo float observations (8, 14–21) and from atmospheric CO₂ measurements at surface stations that are inverted by atmospheric transport models (ATMs) (22–28). These products, however, show a large spread of flux estimates, and are limited by sparse observations, possible measurement biases, and uncertainties in near-surface wind speed, gas exchange coefficients, and modeled atmospheric transport.

Recently, Long et al. (1, henceforth Long21) used atmospheric CO₂ observations from a series of global airborne campaigns to estimate the seasonal cycle of SO CO₂ flux of a single region (90°S to 45°S), and reported an annual oceanic uptake of 0.53±0.23 PgC yr⁻¹ averaged from 2009 to 2018. This annual sink estimate is consistent with the average of atmospheric inversion products (henceforth 3-D inversions) and neural-network interpolation of ship-based pCO₂ products (Surface Ocean CO₂ Atlas, SOCAT) (16, 29), but larger than recent pCO₂-based estimates using neural-network interpolation of profiling floats data from Southern Ocean Carbon and Climate Observations and Modeling project (SOCCOM) (17, 18, 30). Long21 also identified a larger summer-time CO₂ uptake compared to the SOCCOM-based flux estimates and the average of multiple atmospheric inversion products. The method of Long21 uses the atmospheric CO₂ gradient across potential temperature (θ) as an emergent constraint on the underlying air-sea flux, taking advantage of the tendency of CO₂ to be well-mixed on θ surfaces (31).

Here we provide improved estimates of seasonal SO CO₂ flux using a novel 4-box tropospheric inverse method (Fig. 1a, henceforth 4-box inversion) and the same airborne datasets as in Long21 (detailed in Material and Methods and *SI Appendix*, Fig. S1). Whereas Long21 resolved fluxes over a single domain (south of 45°S), our method resolves fluxes in three finer bands ("polar," "subpolar," and "subtropical") between 90°S and ~37°S (Fig. 1b and *SI Appendix*, Fig.

S2), which allows closer comparison with pCO₂-based flux products (16–18) and provides insights into the latitudinal structure of processes driving seasonal pCO₂ changes, such as the interactions between marine photosynthesis, ocean ventilation, and warming/cooling (32, 33).

95

100

105

110

115

120

At mid-latitudes, CO₂ and other long-lived tracers tend to be rapidly dispersed along the surface of constant moist isentrope θ_e , yielding gradients that are roughly parallel to the gradients in θ_e (34–37). Such mixing can be termed "adiabatic mixing", in contrast to "diabatic mixing" which is defined as transport across θ_e surfaces involving diabatic heating or cooling. Our box-model builds on recent work (38, 39) by aligning the box boundaries with fixed values of a massindexed isentropic coordinate $M_{\theta e}$, which is parallel to θ_e at any instant time, but is adjusted to conserve dry air mass in each box. This approach yields box boundaries that are nearly fixed with respect to latitude and season despite large seasonal displacements in θ_e and it highlights diabatic mixing as a critical process for quantifying large-scale tracer dispersion. Atmospheric transport is conventionally determined using ATMs, but these models show a large spread of simulated diabatic transport, which is related to uncertainty in advection, convection, and boundary height parameterizations (24, 40, 41). Prior studies have identified errors in ATMs by pointing to vertical CO₂ gradients being overestimated in simulations at mid-latitude (42, 43). We provide novel estimates of diabatic mixing rates that are independent of ATMs by using the moist static energy (MSE) budget of reanalyses. As MSE surfaces are identical to θ_e and $M_{\theta e}$ surfaces, which are all conserved during adiabatic processes, MSE-based mixing rates provide precise constraints on cross- $M_{\theta e}$ diabatic transport.

In this paper, we start by describing and validating the $M_{\theta e}$ -aligned box-model inversion method. We conduct a systematic analysis of uncertainty in ATMs-simulated diabatic mixing rates across three $M_{\theta e}$ surfaces over the mid- to high-latitude SO by developing two relevant constraints, one based on moist static energy (MSE) budgets and the other based on atmospheric CO_2 gradients across $M_{\theta e}$ surfaces. We present our airborne-based seasonal flux estimates resolved from the box-model inversion method that is constrained by MSE-based diabatic mixing rates, and discuss key features and mechanisms that cause the flux cycles to vary meridionally. Estimates obtained from airborne measurements are further compared with other flux products to identify any limitations these products may have. We also discuss the broad implications of our method for

resolving decadal variability and long-term trends in SO CO₂ fluxes, resolving surface fluxes of other species and in other regions, and the potential to improve ATMs in general.

Results and discussion

125

130

135

140

145

150

Box-model Architecture and Evaluation

The 4-box inversion model, shown in Figure 1a (detailed in Materials and Methods) divides the troposphere in the Southern Hemisphere into discrete boxes, with lateral boundaries aligned with fixed values of $M_{\theta e}(38)$. The $M_{\theta e}$ coordinate is aligned with θ_e , but a given $M_{\theta e}$ surface constantly adjusts to keep the total dry airmass under it conserved. Each $M_{\theta e}$ surface is indexed to the corresponding contained airmass. The three primary boxes of the model each contain 15×10^{16} kg of dry air, and intersect the surface of the Earth in zonal bands (Fig. 1b). The northern-most fourth box provides a boundary condition for the third box. The CO₂ flux at the bottom of each primary box is calculated from mass balance, based on diagnosed CO2 transport between boxes and observed inventory changes within the boxes (Eq. 1). A key assumption of the 4-box model is that the adiabatic transport (along θ_e or $M_{\theta e}$ transport) is sufficiently rapid that CO_2 meridional transport is mainly controlled by bi-directional diabatic transport (across θ_e or $M_{\theta e}$ transport) between boxes, thus effectively reducing the troposphere to a discrete 1-dimensional mixing system. This assumption and the performance of the box model are validated below. In this model, diabatic transport is parameterized based on the cross-M_{θe} CO₂ gradient and a seasonallydependent diabatic mixing rate, expressed in kg² day⁻¹ (Eq. 2). Because airmass (kg) has replaced latitude or length in our box model, these mixing rates are analogous to diffusion coefficients, with the advantage of representing fundamental properties of the atmosphere that are independent of model discretization. We provide two approaches (Materials and Methods) to calculate climatological monthly diabatic mixing rates, one based on CO₂ inversion systems that are constrained by surface CO₂ observations and transport model simulations (ATM-based mixing rates), and one based on moist static energy budgets derived from MERRA-2 and JRA-55 reanalyses (MSE-based mixing rates). We validate the 4-box inversion approach by applying the method to reconstruct surface CO₂ fluxes from 4 CO₂ inverse models, using the full 3-D gridded atmospheric CO₂ fields of each product, averaged over each box, and using the corresponding parameterized climatological ATM-based mixing rates from the same model (detailed in Materials and Methods). This method provides an internally consistent system for

each 3-D inversion, and the reconstructed surface fluxes align well with original inverted fluxes over each zonal band (RMSE \leq 0.12 PgC yr⁻¹, Fig. 3a, *SI Appendix*, Fig. S4-S6, *SI Appendix*, Table S1), especially over the climatological seasonal cycle (Fig. 3b). The 4-box inversion also reconstructs the interannual variability (IAV) of fluxes (e.g., Fig. 3a), even though the box-model uses interannually-constant mixing rates, showing that flux IAV can be learned from variations in atmospheric CO₂ gradients, while the impact of IAV in the atmospheric dynamics is relatively small. The method for resolving the zonal-averaged flux is not biased by the representation error (44, 45) that arises from the coarse resolution inverse model, which we verify by successfully reconstructing zonal-averaged air-sea CO₂ flux from a product with finer-scale variability (Materials and Methods, *SI Appendix*, Fig. S16). These validations confirm that the complex 3-dimensional circulation of the atmosphere at high southern latitudes can be approximated by mixing along one dimension (the coordinate M_{0e}), at least for the purpose of resolving zonal-averaged SO CO₂ fluxes.

Diabatic Mixing Rate Evaluation

155

160

165

170

175

180

We find that the MSE-based mixing rates from MERRA-2 and JRA-55 are highly consistent with each other, while ATM-based mixing rates have a large spread up to threefold, and are faster than MSE-based mixing rates in austral summer over the high-latitudes (Fig. 2 and SI Appendix, Fig. S3). We believe the MSE-based mixing rates are more reliable for two reasons: First, the MSE-based constraint is powerful because surfaces of constant MSE are exactly parallel with the $M_{\theta e}$ coordinate and because MSE has strong gradients across $M_{\theta e}$ in all seasons. Second, the MSE-based constraint is consistent with an additional constraint on mixing that is available when combining CO₂ data from both aircraft and surface stations. The available inverse models compute CO₂ fluxes using surface data only, but also yield troposphere CO₂ gradients which can be compared to airborne observations. We find that the cross- $M_{\theta e}$ CO₂ gradients in most inverse models are inconsistent with the observed gradients in airborne data during the austral summer in the mid- to high-latitude (Fig. 4a and b). The discrepancies in simulated CO₂ gradients correlate strongly with the diagnosed diabatic mixing rates from each corresponding ATM (Fig. 4), showing that ATMs with stronger diabatic mixing produce smaller CO₂ gradients compared to observations. Based on the correlation, we find that the larger observed CO₂ gradients from airborne data than model simulations appear to require a slower mixing rate of ${\sim}10$ and 21 $(10^{16}~kg^2~day^{\text{-1}})$ at the 15 and 30 $M_{\theta e}$ surfaces (Fig. 4a and b), respectively, in the

austral summer. The required mixing rates are consistent with the MSE-based mixing rate, thus providing strong evidence for the MSE-based estimates to be more realistic. Among all ATMs, the ACTM model yields a realistic summer gradient and mixing rates compatible with the MSE budget. In the rest of the year, both MSE-based mixing rates and ATM-based mixing rates, as well as simulated and observed CO_2 gradients are generally within the 1σ uncertainty of the observed gradients and close to two MSE-based mixing rates (*SI Appendix*, Fig. S7).

For the 4-box inversions presented here, we alternately use MSE-based mixing rates derived from MERRA-2 and JRA-55 to invert airborne CO₂ observations, allowing for uncertainty in mixing based on the spread between these two estimates and their small IAV (detailed in *SI Appendix*, Text S2).

Airborne-based air-sea CO2 fluxes

185

190

195

200

205

210

We calculate air-sea CO_2 fluxes using the observed CO_2 inventory of each M_{0e} box and CO_2 gradients across M_{0e} surfaces from each airborne campaign, which are resolved by binning airborne data into four M_{0e} bands (detailed in Materials and Methods). We correct for small biases in CO_2 inventory and gradient induced by sparse spatial coverage of the airborne observations (*SI Appendix*, Text S1 and Table S5) by comparing averaged CO_2 from full 3-D model data and flight track-subsampled model data. We also correct the contribution of small non-oceanic CO_2 flux to the CO_2 mass balance based on flux estimates in four inversion products (*SI Appendix*, Figure S8). Our fluxes estimate allow for uncertainties from CO_2 measurement imprecision, spread and IAV of MSE-based diabatic mixing rates, spatial coverage corrections, flux interannual variability due to insufficient temporal sampling, and non-oceanic CO_2 flux corrections (*SI Appendix*, Text S1-2). Although we report a similar random error as Long21, we expect our results to be subject to smaller systematic errors from uncertainty in mixing, and importantly also allow resolving fluxes at finer spatial scales with the same data. The reported random error is dominated by CO_2 measurement error derived from comparing different instruments.

The 4-box inversion resolves clear seasonal cycles of air-sea CO₂ flux in all three latitude bands, with clear differences in amplitude and phasing between the bands. Over the polar band (Fig. 5a), we find a strong CO₂ uptake in the summer (DJF) and a weak outgassing in the winter (JJA). Over the subpolar band (Fig. 5b), we find a strong uptake in the summer and a weak uptake in

the winter. In the subtropical band (Fig. 5c), the seasonality is reversed, with a weak uptake in the summer and a strong uptake in the rest of the year. Averaged over the full year, all bands show net uptake. We now discuss each of these prominent features in turn.

The airborne-based estimates suggest a weak winter-time CO₂ outgassing of 0.05±0.03 PgC integrated from June to August (equivalent to 0.56±0.35 gC m⁻² mon⁻¹) in the polar band (Fig. 5a). Winter outgassing is expected from strong winter-time upwelling which brings carbon-rich deep water to the surface (13). This outgassing pattern is consistent with several recent pCO₂-based flux estimates, for example, observations from uncrewed surface vehicles in the Antarctic Zone during June and July of 2019 (0.7 gC m⁻² mo⁻¹) (46), reconstructed winter-time (July, 2004-2014 average) fluxes using summer-time measurements (0.04±0.008 PgC) (47), and neural-network interpolation of ship-based SOCAT measurements (0.03 PgC, Fig. 5e) (16), but is smaller than estimates solely based on neural-network interpolation of SOCCOM float data during 2014 and 2017 (~ 0.23 PgC, Fig. 5e). The small winter-time outgassing in our results is also consistent with several 3-D inversions that used surface station CO₂ observations (Jena inversion, ACTM, and CAMS), but is significantly more positive than one 3-D inversion (CT 2019b, Fig. 5e).

The airborne-based flux estimates show a clear phase shift between the polar/subpolar bands (Fig. 5a-b) and the subtropical band (Fig. 5c). The boundary between these two boxes in the 4-box model roughly aligns with the subtropical front over the Atlantic and the Indian Ocean but is ~5° south of the subtropical front over the Pacific Ocean. This phase shift is likely due to the latitudinal change of the dominant mechanism that drives the surface-ocean pCO₂ seasonal changes. To the north of this boundary, the pCO₂ cycle is dominated by temperature-related solubility changes. To the south, it is dominated by biological production/mixing processes driving seasonal changes in dissolved inorganic carbon (32, 33, 48). A similar shift across ~40°S has been resolved in surface ocean pCO₂ data (33, 48, 49) and also in flux estimates based on these pCO₂ data, but the seasonal amplitudes of fluxes in these estimates are weaker in both regions than we find from airborne data (Fig. 5e-g). The phase shift, however, is not distinctly resolved in the 3-D inversions and two neural-network interpolations of pCO₂-based products (Fig. 5e-g).

To quantify the contribution of temperature-related solubility changes to the CO₂ fluxes (Fig. 5i-1), we compare the airborne-based fluxes to results from a simple thermal model, which assumes pCO₂ increases by 4% per degree Celsius increase in sea-surface temperature (SST) change and uses wind-speed dependent gas exchange (methods in *SI Appendix*, Text S3) (50, 51). In the polar zone (Fig. 5i-j), the thermal model yields fluxes that are strongly out of phase compared with observations (correlation $\rho = -0.81$ and -0.83). In the subtropical region (Fig. 5k), the cycle from the thermal model broadly aligns with the observed cycle ($\rho = 0.62$).

Despite the correlation, the observed flux cycle in the subtropical band has significant deviations in the austral spring compared to the thermal-driven cycle. The strengthening of CO₂ uptake from January to April is faster than expected from warming alone (Fig. 5k), which requires a contribution from biological-driven changes, possibly associated with the fall phytoplankton bloom (52, 53).

We find a summer-time ocean CO_2 uptake of 0.13 ± 0.04 PgC (integrated from December to February, DJF) in the polar band (Fig. 5a) and 0.14 ± 0.04 PgC in the subpolar band (Fig. 5b), which contributes to most of the annual uptake of 0.36 ± 0.16 PgC south of ~43°S (Fig. 5d). Our results are qualitatively consistent with prior estimates using the same airborne observations (Long21). However, our annual uptake estimate integrated over the polar and subpolar band is smaller (within uncertainty) than that of Long21 (0.53 ± 0.23 PgC) (Fig. 5d). The difference is mainly explained by larger summer-time CO_2 uptake in Long21, but the comparison is complicated by small differences in ocean domains between these two studies (the 30 $M_{\theta e}$ surface, compared to 45°S, displaces ~2° southward over the western Pacific and ~3° in other basins). The larger summer uptake in Long21 can be attributed to the dependence on ATMs, which we suggest have unrealistically fast mixing rates in summer (Fig. 2). Summertime fluxes from our box model are especially sensitive to the diabatic mixing rate because summertime cross- $M_{\theta e}$ gradients are large, and the inventory change is small (Fig. 4). The winter-time fluxes are less sensitive to the diabatic mixing rate because wintertime CO_2 gradients are small, and the inverted flux is mainly diagnosed from the observed atmospheric CO_2 inventory change.

In the two high-latitudes band (Fig. 5e-f), our flux estimates align better with the SOCAT-based flux estimate than the SOCCOM-based estimate. We find that the SOCCOM-based flux estimates show significantly larger CO₂ outgassing (or weaker uptake) all year round. Possible

bias in SOCCOM pCO₂ data has been identified by Wu et al. (54), and SOCCOM float data remain sparse in our lowest latitude band 43-37°S (18).

Our airborne-based estimates show large differences from global ocean biogeochemistry models, which have known difficulties in representing CO₂ exchange over the Southern Ocean (8, 55, 56) given the large competing process drivers. We find several models that suggest a similar phase shift, but we did not find any model that agrees well with our estimates in all three bands (*SI Appendix*, Fig. S9). Airborne-based estimates are relatively consistent with pCO₂-based estimates and inversions, while sharply deviating from GOBMs, underscoring the need for a better understanding of the physical and biogeochemical processes that drive the SO air-sea CO₂ flux in GOBMs.

Overview and outlook

275

280

285

290

295

300

We have resolved air-sea CO₂ fluxes over three zonal bands of the SO using airborne data and a 4-box inversion approach based on M_{0e} coordinates. This framework adequately describes large-scale CO₂ transports needed for resolving fluxes at the scale of three zonal bands over the midto high latitudes of the SO, showing that the complex meridional CO₂ transport can be simplified to diabatic transport. This framework also incorporates constraints on the diabatic mixing rate from MSE budgets of atmospheric reanalyses, without requiring an atmospheric transport model. We demonstrate that the diabatic mixing rates inferred from the MSE budgets are realistic, based on a CO₂ gradient-mixing rate constraint, but the mixing in most ATMs is too fast in the austral summer. These differences in representing mixing led to our summer uptake estimates being somewhat smaller than the uptake estimated by Long21, despite using the same airborne CO₂ data. In the austral winter, ATM- and MSE-based mixing rates are generally comparable.

This study provides robust zonal average flux estimates from airborne data by capitalizing on rapid atmospheric mixing to integrate zonal heterogeneities. Our estimates have advantages over the published atmospheric inversions using surface station data because airborne data more accurately reflect large-scale features, and our method is less sensitive to large uncertainty in simulated atmospheric mixing and the representation error due to model resolution (44). Compared to pCO₂-based products, our estimates also have advantages, not being subject to uncertainty in gas exchange velocity and sparse coverage in pCO₂ observations (1, 21). A corresponding disadvantage, however, is the inability to resolve finer-scale spatial features.

The 4-box inverse model provides insights that have potential value for understanding and improving the simulated atmospheric circulation and structure in 3-D ATMs. We show inconsistency in MSE-based and ATM-based diabatic mixing rates, and in CO₂ gradients between airborne data and inversion systems that are optimized by surface data (Fig. 4). These inconsistencies strongly motivate the incorporation of airborne data into CO₂ inversion systems. They also identify key errors during the construction of modern ATMs related to diabatic mixing. Previous studies have highlighted uncertainty in vertical mixing as a major source of error in CO₂ fluxes estimated via inverse model calculations using both satellite and in situ data (42, 43). Vertical mixing in the mid-troposphere has both along- and cross- $M_{\theta e}$ components, and the cross- $M_{\theta e}$ mixing (diabatic) component would typically be rate limiting because the along- $M_{\theta e}$ (adiabatic) mixing is more rapid. Reducing uncertainty in vertical mixing thus requires reducing uncertainty in diabatic mixing, which we show can be constrained with MSE budgets. Future studies should focus on better understanding the inconsistency between transport models and reanalyses, which likely are associated with insufficient vertical resolutions, uncertainty in parameterizations (e.g., convection), and challenges related to the re-gridding and interpolation when assimilating meteorology data into these models.

Our study motivates obtaining additional airborne data to improve estimates of large-scale carbon uptake across different latitudes of the SO. The ocean uptake over the entire SO has increased in recent decades according to surface ocean pCO₂ data and models (2, 7–9, 11–13, 21). Here we only attempted to resolve a seasonal climatology of the SO CO₂ flux over different latitudes over the period 2009-2018, but resolving interannual variation would be feasible given regular sampling on future aircraft campaigns, with spatial coverage over the SO similar to HIPPO, ORCAS, and ATom. New frameworks based on the $M_{\theta e}$ coordinate are suitable also for studying the sources and sinks of other tracers, for example, computing the air-sea O₂ flux, and atmospheric CH₄ chemical loss rate.

Materials and methods

305

310

315

320

325

330

Airborne campaigns and airborne CO₂ observations

We use airborne CO_2 observations from three aircraft campaigns, the HIAPER Pole-to-Pole Observation project (HIPPO, (57)), the O_2/N_2 Ratio and CO_2 Airborne Southern Ocean Study (ORCAS, (58)), and the Atmospheric Tomography Mission (ATom, (59)). HIPPO and ATom

have global coverage, mostly along a Pacific or Atlantic transect, while ORCAS focused on the Southern Ocean adjacent to Drake Passage (horizontal flight tracks are shown in *SI Appendix*, Fig. S1). HIPPO consisted of five campaigns (HIPPO1-5) and ATom consisted of four campaigns (ATom1-4), each with several flights south of 35°S. ORCAS was a single 6-week campaign, but with much denser temporal sampling, so we have split it into three sub-campaigns (ORCAS1-3) in our analysis. Detailed descriptions of these airborne campaigns are in *SI Appendix*, Text S4 and *SI Appendix*, Table S2. We primarily use CO₂ airborne measurements collected by the NCAR AO2 instrument (60). To evaluate potential uncertainty (detailed in *SI Appendix*, Text S2.1), we also use measurements from three other in-situ instruments, the Harvard QCLS instrument (61), Harvard OMS instrument (62), and NOAA Picarro, and measurements from two flask samplers, the NCAR/Scripps Medusa flask sampler (60, 63) and NOAA Portable Flask Packages(PFP, 63). AO2 and QCLS are available on all campaigns. However, OMS did not fly on ORCAS or ATom, NOAA PFPs did not fly on ORCAS, and the NOAA Picarro did not fly on HIPPO. The in-situ measurements are averaged to 10-sec intervals.

Mass-indexed moist isentropic coordinate ($M_{\theta e}$)

335

340

345

350

355

360

The $M_{\theta e}$ coordinate, first introduced in Jin et al. (38), is defined as the total dry air mass under a specific moist isentropic surface (θ_e) in the troposphere of a given hemisphere. Surfaces of constant $M_{\theta e}$ align with surfaces of constant θ_e but the relationship changes with season, as the atmosphere warms and cools. A schematic of the annual zonal average atmospheric $M_{\theta e}$ value is in shown Fig. 1a, while climatological positions of the near-Earth surface contours of three $M_{\theta e}$ surfaces (15, 30, and 45 10^{16} kg) are shown in Fig. 1b and *SI Appendix*, Fig. S2. Details of the calculation of $M_{\theta e}$ are described in *SI Appendix*, Text S5.

We also relate bands of constant $M_{\theta e}$ to approximate latitude bands (see Fig. 5) based on the zonal average latitude of corresponding daily surface $M_{\theta e}$ (averaged from 2009 to 2018) over the ocean.

Box model architecture and diabatic mixing rates

We build a 4-box atmospheric model using selected $M_{\theta e}$ surfaces (15, 30, 45, and 60, 10^{16} kg) as boundaries, shown in Fig. 1a. This box model takes advantage of θ_e (or $M_{\theta e}$) being the preferential mixing surface of CO_2 throughout the hemisphere, especially over mid-latitude storm tracks (34, 37). The box model allows surface CO_2 fluxes (F_i , PgC year⁻¹) to be computed

from the CO_2 mass balance of each $M_{\theta e}$ box, based on the knowledge of atmospheric CO_2 inventory (M_i , PgC) in each box and the diabatic transport of CO_2 between boxes ($Q_{i,i+1}$, PgC year⁻¹)

$$\frac{\partial M_{i}}{\partial t} = \begin{cases} F_{i} + Q_{i,i+1} & \text{if } i = 1\\ F_{i} + Q_{i,i+1} - Q_{i-1,i} & \text{if } i > 1 \end{cases}$$
 (1)

where i = 1 is the highest latitude (lowest $M_{\theta e}$) box.

365

380

385

In Eq.1, $Q_{i,i+1}$ represents the transport (PgC year⁻¹) of CO_2 between the i^{th} and $i+1^{th}$ box, with poleward flux as positive. $Q_{i,i+1}$ is parameterized according to:

$$Q_{i,i+1} = D_{i,i+1} \cdot \frac{(\chi_{i+1} - \chi_i)}{\Delta M_{\theta_e}} \cdot \kappa$$
 (2)

where D_{i,i+1} is the diabatic mixing rate (kg² day⁻¹) that represents the mixing rate across the boundary of box i and i+1, χ_i is the CO₂ concentration (PgC per kg air mass) of the ith box, calculated as CO₂ inventory of the box divided by the total airmass of the box (15×10¹⁶ kg), and ΔM_{θe} is the distance in M_{θe} coordinates between box centers, which for evenly spaced boxes is the same as the total airmass of each box. κ is a constant (1/365) to convert from PgC day⁻¹ to PgC year⁻¹. Equation 2 is a variant of Fick's law, with M_{θe} as an effective distance coordinate, and $\frac{(\chi_{i+1}-\chi_i)}{\Delta M_{\theta_e}}$ is a measure of the CO₂ concentration gradient. With this approach, D_{i,i+1} is a property of the corresponding M_{θe} surface and is insensitive to the choice of box size.

We adopt two independent methods to estimate climatological (2009 to 2018 average) monthly diabatic mixing rates ($D_{i,i+1}$). The first method extracts diabatic mixing rates from transport models using total CO_2 fields from 3-D inversion products (*SI Appendix*, Table S3). We first use the daily 3-D atmospheric field of $M_{\theta e}$ computed from MERRA-2 to assign a $M_{\theta e}$ value to each daily model grid cell from 2009 to 2018. The atmospheric 3-D CO_2 fields and surface CO_2 flux fields of inversions are interpolated to the MERRA-2 reanalysis grids ($1^{\circ}x1^{\circ}$, 26 vertical levels from 1000 mbar to 100 mbar). We then calculate a daily CO_2 inventory (M_i) of each $M_{\theta e}$ band as the sum of CO_2 mass for all 3-D grid boxes within the corresponding $M_{\theta e}$ domain. We calculate monthly CO_2 inventory change ($\frac{dM_i}{dt}$) by taking the time derivative of the monthly atmospheric CO_2 inventory. We note that monthly CO_2 inventory change is computed by first averaging daily

 CO_2 inventory by month but shifting the phase of the averaging window by 15 days to center at the beginning of each month, and then differencing these values to obtain a rate of change centered mid-month. We calculate monthly CO_2 gradients between two $M_{\theta e}$ boxes $(\chi_{i+1}-\chi_i)$ by averaging daily gradients. We calculate monthly surface CO_2 flux (F_i) by averaging daily flux, which is computed by integrating all daily 3-D inversion flux grids with surface $M_{\theta e}$ values within the corresponding $M_{\theta e}$ range.

390

395

400

405

410

The CO₂ transport across the north boundary of each $M_{\theta e}$ box in the model can be calculated from the CO₂ inventory change and surface flux of that box and the boxes further southward, according to:

$$Q_{i,i+1}(t) = \sum_{i'=1}^{i'=i} \left(\frac{dM_{i'}(t)}{dt} - F_{i'}(t) \right)$$
 (3)

Combining Eq. 2 and 3, climatological average (2009 to 2018 average) monthly $D_{i,i+1}$ is calculated following:

$$D_{i,i+1}(t) = \frac{\left[\sum_{i'=1}^{i'=i} \left(\frac{dM_{i'}(t)}{dt} - F_{i'}(t)\right)\right]}{\left[\chi_{i+1}(t) - \chi_{i}(t)\right]} \cdot \Delta M_{\theta_{e}}$$
(4)

where [] denotes the average of corresponding monthly values of all years (2009 to 2018). The 1σ uncertainty is calculated as the standard deviation of resolved $D_{i,i+1}(t)$ for that month over all years, representing the interannual variability, which is shown to be small (Fig. 2 and *SI Appendix*, Fig. S3), with the exception of CAMS in September because of close-to-zero CO_2 gradients across the 30 (10^{16} kg) $M_{\theta e}$ surface.

The second method relies on moist static energy (MSE) budgets from meteorological reanalyses, of which we use MERRA-2 and JRA-55 (65, 66). MSE is a measure of static energy that is conserved in adiabatic ascent/descent and during latent heat release due to condensation, and is thus aligned with surfaces of θ_e or $M_{\theta e}$. This method provides a much more well-defined D because finite MSE gradients exist in each reanalysis time step and do not reverse sign, in contrast to CO_2 . MSE is defined following

$$MSE(t) = C_p \cdot T(t) + g \cdot z + L_v(T) \cdot q(t)$$
 (5)

where C_p (1005.7 J kg⁻¹ K⁻¹) is the specific heat of dry air at a constant pressure, T is temperature (K), g is the gravity constant assumed to be 9.81 m s⁻², q is the specific humidity of air (kg water vapor per kg air mass), and L_v is the latent heat of evaporation at temperature T (K). L_v is defined as 2406 kJ kg⁻¹ at 40°C and 2501 kJ kg⁻¹ at 0°C and scales linearly with temperature.

415

420

425

430

435

MSE transport at the northern boundary of each box is calculated by energy conservation within the box, which follows Eq. 3 but has a small modification to account for atmospheric energy sources or sinks (E_i , J day⁻¹):

$$Q_{i,i+1}(t) = \sum_{i'=1}^{i'=i} \left(\frac{dS_{i'}(t)}{dt} - F_{i'}(t) - E_{i'}(t) \right)$$
 (6)

where S is the total MSE (J) that is calculated using temperature (T) and specific humidity (q) from corresponding reanalyses (Eq. 5). F_i is modified as surface heat flux (J day⁻¹), including surface sensible and latent heat flux, which is directly available from MERRA-2 and JRA-55. E_i is defined as heating rate due to radiative imbalance, and is calculated using temperature tendency analysis ($\frac{\partial T_i}{\partial t}$, K day⁻¹) of these reanalyses, following:

$$E_{i}(t) = C_{p}(T) \cdot \frac{\partial T_{i}(t)}{\partial t} \cdot M_{\theta_{e}}$$
 (7)

With MERRA-2, the temperature tendency due to radiative imbalance is directly available, while with JRA-55, it is calculated as the sum of heating rates due to longwave and shortwave radiation.

To estimate climatological monthly $D_{i,i+1}$ from reanalysis, the gradient $(\chi_{i+1} - \chi_i)$ in Eq. 4 is modified to be the energy density gradient (J per kg airmass), calculated from the total MSE of each box divided by the total airmass of the box $(15 \times 10^{16} \text{ kg in this study})$.

We thus calculate monthly $\frac{dS_{i'}(t)}{dt}$, $F_{i'}(t)$, $E_{i'}(t)$ from 2009 to 2018 by averaging 6-hourly data from MERRA-2 and JRA-55, with 6-hourly S_i shifted by 15 days before calculating $\frac{dS_{i'}(t)}{dt}$, as for ATM CO₂.

The calculation of monthly D based on MSE is according to a modified version of Eq. 4:

$$D_{i,i+1}(t) = \frac{\left[\sum_{i'=1}^{i'=i} \left(\frac{dS_{i'}(t)}{dt} - F_{i'}(t) - E_{i'}(t)\right)\right]}{\left[\chi_{i+1}(t) - \chi_{i}(t)\right]} \cdot \Delta M_{\theta_{e}}$$
(8)

We show six (four ATM-based and two MSE-based) sets of monthly diabatic mixing rates for the $M_{\theta e}$ surfaces at 15, 30, and 45 (10¹⁶ kg) in Fig. 2 and *SI Appendix*, Fig. S3. Climatological daily mixing rates are further calculated by 4-harmonic fits to monthly data.

Validation of box-model approach

445

450

455

460

465

We validate the use of the 4-box model for estimating surface CO_2 flux by showing that this approach successfully reconstructs monthly surface CO_2 fluxes for each of the four 3-D CO_2 inversion products. This approach uses Eq. 1 and 2, with χ_i based on the gridded atmospheric CO_2 fields averaged over grid cells within corresponding $M_{\theta e}$ box and uses $D_{i,i+1}$ calculated using CO_2 gradients from each transport model as described in the previous section. We then average daily reconstructed fluxes to monthly, centered at the middle of each month, shown as solid black curves in Fig. 3 and *SI Appendix*, Fig. S4-S6. We assess representation error due to the coarse resolution of the inverse model, by reconstructing the zonal average flux of the neural-network interpolation of SOCAT data, using the 3D atmospheric field generated by the TM3 model with flux from SOCAT-based air-sea CO_2 flux, together with fossil fuel and ecosystem CO_2 flux from the Jena sEXTocNEEv2020 (*SI Appendix*, Fig. S16). We find clear alignment between the original and reconstructed SOCAT-based flux, suggesting that our method is not limited by representation error.

Airborne estimates of air-sea CO₂ fluxes

We use the 4-box model (Eq. 1 & 2) and airborne CO_2 observations to calculate air-sea CO_2 fluxes for each surface $M_{\theta e}$ band and each airborne campaign, centering on the mean date of the campaign, shown as points in Figure 5a-d. This calculation includes the following steps.

We first detrend airborne CO₂ observations by subtracting a smoothed interannual CO₂ trend at the South Pole (SPO) (67). The trend is calculated by a stiff cubic spline function to the monthly average SPO data (68). We then compute the detrended average CO₂ ($\hat{\chi}_i$) for each campaign and each box by trapezoidal integration of detrended CO₂ as a function of M_{θe} (as in Jin et al. (38)), and dividing by the M_{θe} range of the box (i.e., 15×10¹⁶ kg) (68). Prior to trapezoidal integration, we extrapolate airborne observations to M_{θe} = 0 surface using the average of the 100

observations with the lowest $M_{\theta e}$ values near 0. The extrapolation only results in a slightly different averaged CO₂ for the lowest $M_{\theta e}$ box compared to the value without extrapolation (< 0.03 ppm) because we have sufficient measurements across $M_{\theta e}$ surfaces. The exceptions are HIPPO1 and 4 (difference ≈ 0.1 ppm), in which we do not have observations on low $M_{\theta e}$ surfaces (SI Appendix, Fig. S15). For HIPPO4, however, we extrapolate to $M_{\theta e} = 15~(10^{16}~kg)$ using the average of the 100 observations with the lowest $M_{\theta e}$ values near 15 because due to the absence of observations in the entire first M_{0e} box, and only estimate fluxes for the 30-45 (10¹⁶ kg) box. We then correct for bias in CO₂ estimates due to limited spatial coverage (detailed in SI Appendix, Text S1). For each $M_{\theta e}$ box, we conduct a 2-harmonic fit with an annual offset to $\hat{\chi}_i$ of 12 campaigns, yielding a fitted seasonal cycle (with offset) of $\hat{\chi}_i$. We then compute the long-term (2009 to 2018) time series of observed χ_i as the sum of the climatological seasonal cycle of $\widehat{\chi}_i$ and the CO₂ trend at SPO. We note that we use the same trend for each $M_{\theta e}$ band, preserving each band's annual mean offset from SPO. The time series of CO2 inventory (Mi) of each box is therefore computed by multiplying χ_i and the $M_{\theta e}$ range of the box (i.e., 15×10^{16} kg in this study). The Fitted χ_i and M_i values of each campaign are defined as the values at the mean date of the corresponding campaign. Observed surface CO2 fluxes for each airborne campaigns are then calculated as the combination of two components, namely the CO₂ inventory change $\frac{\partial M_i}{\partial t}$ and CO₂ diabatic transport $Q_{i,i+1}$, following Eq. 1 and 2. We calculate the component $\frac{\partial M_i}{\partial t}$ as the time derivative of the daily timeseries of M_i from the combined seasonal plus SPO trend fit. The component Qi,i+1 for each airborne campaign mean date is calculated as the product of the observed atmospheric CO₂ gradient (without fitting) between two boxes and the 4-harmonic fitted diabatic mixing rate at the campaign mean date (average of 2 MSE-based mixing rates) of the corresponding $M_{\theta e}$ surface.

470

475

480

485

490

The surface CO₂ fluxes estimated from the 4-box model are the total fluxes that also contain any land ecosystem CO₂ emission/uptake and fossil fuel CO₂ emission. We correct for these non-oceanic components by subtracting the corresponding flux components using the average of four 3-D CO₂ inversion products. The magnitude of this correction is small compared to the total airsea fluxes, as shown in *SI Appendix*, Fig. S8.

We estimate the uncertainty of each individual flux estimate and the seasonal flux cycle by generating an ensemble (2000 iterations) of flux estimates, allowing for uncertainty of these sources: (1) uncertainty of CO₂ measurements; (2) uncertainty of the correction for spatial bias due to insufficient airborne coverage; (3) interannual variability of the diabatic mixing rate; (4) spread of the diabatic mixing rate between the two reanalyses; (5) correction for the biosphere and fossil fuel CO₂ flux; and (6) interannual variability of the flux. Detailed bias and uncertainty analyses are presented in *SI Appendix*, Text S1-2. The overall uncertainties of each flux estimate are shown as error bars in Fig. 5a-d. The overall uncertainties of 2-harmonic fitted seasonal flux cycles are shown as shaded regions in Fig. 5a-d.

We also show the averaged air-sea CO_2 fluxes calculated using 6 sets of diabatic mixing rates (4 sets of ATM-based and 2 sets of MSE-based) in *SI* Appendix, Fig. S10. These are estimated using the average and 1σ uncertainty of 6000 iterations of flux estimates, with 1000 iterations for each set of mixing rates. We also show the air-sea CO_2 fluxes calculated using each set of mixing rates in *SI* Appendix, Fig. S11.

We calculate the annual CO_2 uptake of each $M_{\theta e}$ box from the constant term of the 2-harmonic fitted seasonal flux cycles (shown as text in Fig. 5).

510 Acknowledgement

495

500

505

515

520

We thank the efforts of the full HIPPO, ORCAS, and ATom science teams and the pilots and crew of the NSF/NCAR GV and NASA DC-8 as well as the NCAR and NASA project managers, field support staff, and logistics experts. In this work, we have used the HIPPO, ORCAS, and ATom 10-s merge files. We thank the NCAR AO2, Harvard QCLS, Harvard OMS, NOAA UCATS, and NOAA Picarro, NOAA PFP, and NCAR/Scripps Medusa teams for sharing CO₂ measurements. These include Sara Afshar, Jonathan Bent, John Budney, Róisín Commane, Bruce Daube, Glenn Diskin, Rodrigo Jimenez, Kathryn McKain, Fred Moore, Tim Newberger, Jasna Pittman, Bill Paplawsky, Sunyoung Park, Greg Santoni, Stephen Shertz, MacKenzie Smith, Andy Watt, Steven Wofsy, and Bin Xiang. For sharing O₃, N₂O, and H₂O measurements, we also thank Jim Elkins, Eric Hintsa, and Fred Moore for ATom-1 N₂O data; Ru-Shan Gao and Ryan Spackman for HIPPO O₃ data; Ilann Bourgeois, Jeff Peischl, Tom Ryerson, and Chelsea Thompson for ATom O₃ data; Stuart Beaton, Minghui Diao, and Mark Zondlo for HIPPO and ORCAS H₂O data; and Glenn Diskin and Josh DiGangi for ATom H₂O data.

Yuming Jin was supported under a grant from NSF (AGS-1623748) and under a grant from Earth Networks. This material is based on work supported by the National Center for 525 Atmospheric Research, which is a major facility sponsored by the NSF under Cooperative Agreement No. 1852977. HIPPO was supported by NSF grants ATM-0628575, ATM-0628452, ATM-0628519, and ATM-0628388. ORCAS was supported by grants NSF PLR-1501993, PLR-1502301, PLR-1501997, and PLR-1501292. ATom was supported by NASA grant NNX15AJ23G. The NOAA CO₂ ATom measurements were supported by NASA grant 530 NNX16AL92A. NCAR and Scripps AO2 and Medusa measurements in ATom were supported by NSF AGS-1547626 and AGS-1547797 for ATom1 and by NSF AGS-1623745 and AGS-1623748 for ATom 2-4. Recent CO₂ measurements at SPO station have been supported by NASA (NNX17AE74G) and by Eric and Wendy Schmidt via recommendation of the Schmidt Futures program. We also thank two anonymous reviewers for the valuable comments and 535 efforts. Any opinions, findings, conclusions, and recommendations expressed in this material are those of the authors and do not necessarily reflect the views of NSF, NOAA, or DOE.

References

- 1. M. C. Long, *et al.*, Strong Southern Ocean carbon uptake evident in airborne observations. *Science*. **374**, 1275–1280 (2021).
 - 2. N. Gruber, *et al.*, The oceanic sink for anthropogenic CO₂ from 1994 to 2007. *Science*. **363**, 1193–1199 (2019).
 - 3. J. Hauck, *et al.*, On the Southern Ocean CO2 uptake and the role of the biological carbon pump in the 21st century. *Global Biogeochem. Cycles* **29**, 1451–1470 (2015).
- 4. A. Kessler, J. Tjiputra, The Southern Ocean as a constraint to reduce uncertainty in future ocean carbon sinks. *Earth Syst. Dyn.* 7, 295–312 (2016).
 - 5. N. S. Lovenduski, G. A. McKinley, A. R. Fay, K. Lindsay, M. C. Long, Partitioning uncertainty in ocean carbon uptake projections: Internal variability, emission scenario, and model structure. *Global Biogeochem. Cycles* **30**, 1276–1287 (2016).
- 550 6. M. Gloor, *et al.*, A first estimate of present and preindustrial air-sea CO₂ flux patterns based on ocean interior carbon measurements and models. *Geophys. Res. Lett.* **30** (2003).

- 7. J. Yun, *et al.*, Enhance seasonal amplitude of atmospheric CO2 by the changing Southern Ocean carbon sink. *Sci. Adv.* **8** (2022).
- 8. K. B. Rodgers, *et al.*, Seasonal Variability of the Surface Ocean Carbon Cycle: A Synthesis. *Global Biogeochem. Cycles* **37**, e2023GB007798 (2023).
 - 9. N. S. Lovenduski, N. Gruber, S. C. Doney, Toward a mechanistic understanding of the decadal trends in the Southern Ocean carbon sink. *Global Biogeochem. Cycles* **22**, GB3016 (2008).
- 10. C. D. Nevison, *et al.*, Southern Annular Mode Influence on Wintertime Ventilation of the Southern Ocean Detected in Atmospheric O₂ and CO₂ Measurements. *Geophys. Res. Lett.* 47, e2019GL085667 (2020).
 - 11. P. Friedlingstein, et al., Global Carbon Budget 2020. Earth Syst. Sci. Data 12, 3269–3340 (2020).
- 12. C. Le Quéré, *et al.*, Saturation of the southern ocean CO₂ sink due to recent climate change. *Science.* **316**, 1735–1738 (2007).
 - 13. N. Gruber, P. Landschutzer, N. S. Lovenduski, The Variable Southern Ocean Carbon Sink. *Ann. Rev. Mar. Sci.* **11**, 159–186 (2019).
 - 14. L. Gregor, S. Kok, P. M. S. Monteiro, Interannual drivers of the seasonal cycle of CO₂ in the Southern Ocean. *Biogeosciences* **15**, 2361–2378 (2018).
- 570 15. P. Landschützer, N. Gruber, D. C. E. Bakker, U. Schuster, Recent variability of the global ocean carbon sink. *Global Biogeochem. Cycles* **28**, 927–949 (2014).
 - 16. P. Landschützer, N. Gruber, D. C. E. Bakker, Decadal variations and trends of the global ocean carbon sink. *Global Biogeochem. Cycles* **30**, 1396–1417 (2016).
- 17. P. Landschützer, S. M. Bushinsky, A. R. Gray, A combined globally mapped carbon dioxide (CO2) flux estimate based on the Surface Ocean CO2 Atlas Database (SOCAT) and Southern Ocean Carbon and Climate Observations and Modeling (SOCCOM) biogeochemistry floats from 1982 to 2017 (NCEI Accession 0191304), (2019) https://doi.org/10.25921/9hsn-xq82.

- 18. S. M. Bushinsky, *et al.*, Reassessing Southern Ocean Air-Sea CO₂ Flux Estimates With the Addition of Biogeochemical Float Observations. *Global Biogeochem. Cycles* **33**, 1370–1388 (2019).
 - 19. R. Ritter, *et al.*, Observation-Based Trends of the Southern Ocean Carbon Sink. *Geophys. Res. Lett.* **44**, 12339–12348 (2017).
- 20. C. Rödenbeck, *et al.*, Data-based estimates of the ocean carbon sink variability First results of the Surface Ocean pCO₂ Mapping intercomparison (SOCOM). *Biogeosciences* 12, 7251–7278 (2015).
 - 21. T. DeVries, *et al.*, Magnitude, trends, and variability of the global ocean carbon sink from 1985-2018. *Global Biogeochem. Cycles* **37**, e2023GB007780 (2023).
- C. Rödenbeck, S. Houweling, M. Gloor, M. Heimann, CO₂ flux history 1982–2001 inferred from atmospheric data using a global inversion of atmospheric transport. *Atmos. Chem. Phys.* 3, 1919–1964 (2003).
 - 23. A. R. Jacobson, et al., CarbonTracker CT2019B (2020) https://doi.org/10.25925/20201008.
 - 24. P. K. Patra, *et al.*, Improved chemical tracer simulation by MIROC4.0-based atmospheric chemistry-transport model (MIROC4-ACTM). *Sci. Online Lett. Atmos.* **14**, 91–96 (2018).
- 595 25. N. Chandra, *et al.*, Estimated regional CO₂ flux and uncertainty based on an ensemble of atmospheric CO₂ inversions. *Atmos. Chem. Phys.* **22**, 9215–9243 (2022).
 - 26. F. Chevallier, *et al.*, Inferring CO₂ sources and sinks from satellite observations: Method and application to TOVS data. *J. Geophys. Res. Atmos.* **110**, D24309 (2005).
- F. Chevallier, On the parallelization of atmospheric inversions of CO₂ surface fluxes within a variational framework. *Geosci. Model Dev.* **6**, 783–790 (2013).
 - 28. F. Chevallier, *et al.*, CO₂ surface fluxes at grid point scale estimated from a global 21 year reanalysis of atmospheric measurements. *J. Geophys. Res. Atmos.* **115**, D21307 (2010).
 - 29. D. C. E. Bakker, et al., An update to the surface ocean CO₂ atlas (SOCAT version 2). Earth Syst. Sci. Data 6, 69–90 (2014).
- 605 30. K. S. Johnson, et al., Biogeochemical sensor performance in the SOCCOM profiling float

- array. J. Geophys. Res. Ocean. 122, 6416-6436 (2017).
- 31. E. A. Barnes, N. Parazoo, C. Orbe, A. S. Denning, Isentropic transport and the seasonal cycle amplitude of CO₂. *J. Geophys. Res. Atmos.* **121**, 8106–8124 (2016).
- 32. C. J. Prend, J. M. Hunt, M. R. Mazloff, S. T. Gille, L. D. Talley, Controls on the Boundary Between Thermally and Non-Thermally Driven pCO₂ Regimes in the South Pacific. *Geophys. Res. Lett.* **49**, e2021GL095797 (2022).
 - 33. J. L. Sarmiento, N. Gruber, *Ocean Biogeochemical Dynamics* (Princeton University Press, 2006).
- 34. N. C. Parazoo, *et al.*, Moist synoptic transport of CO₂ along the mid-latitude storm track.

 615 *Geophys. Res. Lett.* **38**, L09804 (2011).
 - 35. N. C. Parazoo, A. S. Denning, S. R. Kawa, S. Pawson, R. Lokupitiya, CO₂ flux estimation errors associated with moist atmospheric processes. *Atmos. Chem. Phys.* **12**, 6405–6416 (2012).
- 36. O. Pauluis, A. Czaja, R. Korty, The global atmospheric circulation in moist isentropic coordinates. *J. Clim.* **23**, 3077–3093 (2010).
 - 37. O. Pauluis, A. Czaja, R. Korty, The global atmospheric circulation on moist isentropes. *Science*. **321**, 1075–1078 (2008).
 - 38. Y. Jin, *et al.*, A mass-weighted atmospheric isentropic coordinate for mapping chemical tracers and computing inventories. *Atmos. Chem. Phys.* **21**, 217–238 (2021).
- 425 39. Y. Jin, *et al.*, Seasonal Tropospheric Distribution and Air-Sea Fluxes of Atmospheric Potential Oxygen From Global Airborne Observations. *Global Biogeochem. Cycles* 37, e2023GB007827 (2023).
 - 40. D. A. Belikov, *et al.*, Off-line algorithm for calculation of vertical tracer transport in the troposphere due to deep convection. *Atmos. Chem. Phys.* **13**, 1093–1114 (2013).
- 41. A. E. Schuh, *et al.*, Quantifying the Impact of Atmospheric Transport Uncertainty on CO2 Surface Flux Estimates. *Global Biogeochem. Cycles* **33**, 484–500 (2019).
 - 42. B. B. Stephens, et al., Weak Northern and Strong Tropical Land Carbon Uptake from

- Vertical Profiles of Atmospheric CO₂. Science. **316**, 1732–1735 (2007).
- 43. B. Gaubert, *et al.*, Global atmospheric CO₂ inverse models converging on neutral tropical land exchange, but disagreeing on fossil fuel and atmospheric growth rate. *Biogeosciences* **16**, 117–134 (2019).
 - 44. T. Kaminski, P. J. Rayner, M. Heimann, I. G. Enting, On aggregation errors in atmospheric transport inversions. *J. Geophys. Res. Atmos.* **106**, 4703–4715 (2001).
- 45. T. Janjić, *et al.*, On the representation error in data assimilation. *Q. J. R. Meteorol. Soc.* **144**, 1257–1278 (2018).
 - 46. A. J. Sutton, N. L. Williams, B. Tilbrook, Constraining Southern Ocean CO2 Flux Uncertainty Using Uncrewed Surface Vehicle Observations. *Geophys. Res. Lett.* 48, e2020GL091748 (2021).
- 47. N. Mackay, A. Watson, Winter Air-Sea CO₂ Fluxes Constructed From Summer Observations of the Polar Southern Ocean Suggest Weak Outgassing. *J. Geophys. Res. Ocean.* **126**, e2020JC016600 (2021).
 - 48. P. Landschützer, N. Gruber, D. C. E. Bakker, I. Stemmler, K. D. Six, Strengthening seasonal marine CO₂ variations due to increasing atmospheric CO₂. *Nat. Clim. Chang.* **8**, 146–150 (2018).
- 650 49. K. R. Gurney, *et al.*, Towards robust regional estimates of annual mean CO₂ sources and sinks. *Nature* **415**, 626–630 (2002).
 - 50. T. Takahashi, *et al.*, Climatological mean and decadal change in surface ocean pCO₂, and net sea-air CO₂ flux over the global oceans. *Deep. Res. Part II Top. Stud. Oceanogr.* **56**, 554–577 (2009).
- 655 51. R. Wanninkhof, W. E. Asher, D. T. Ho, C. Sweeney, W. R. McGillis, Advances in Quantifying Air-Sea Gas Exchange and Environmental Forcing. *Ann. Rev. Mar. Sci.* 1, 213–244 (2009).
 - 52. M. J. Behrenfeld, P. G. Falkowski, Photosynthetic rates derived from satellite-based chlorophyll concentration. *Limnol. Oceanogr.* **42**, 1–20 (1997).

- 53. J. K. Moore, M. R. Abbott, Phytoplankton chlorophyll distributions and primary production in the Southern Ocean. *J. Geophys. Res. Ocean.* **105**, 28709–28722 (2000).
 - 54. Y. Wu, *et al.*, Integrated analysis of carbon dioxide and oxygen concentrations as a quality control of ocean float data. *Commun. Earth Environ.* **3**, 92 (2022).
- 55. J. Hauck, *et al.*, Consistency and Challenges in the Ocean Carbon Sink Estimate for the Global Carbon Budget. *Front. Mar. Sci.* **7**, 571720 (2020).
 - 56. A. R. Fay, G. A. McKinley, Observed Regional Fluxes to Constrain Modeled Estimates of the Ocean Carbon Sink. *Geophys. Res. Lett.* **48**, e2021GL095325 (2021).
 - 57. S. C. Wofsy, HIAPER Pole-to-Pole Observations (HIPPO): fine-grained, global-scale measurements of climatically important atmospheric gases and aerosols. *Philos. Trans. R. Soc. A Math. Phys. Eng. Sci.* **369**, 2073–2086 (2011).

- 58. B. Stephens, *et al.*, The O₂/N₂ ratio and CO₂ airborne Southern Ocean study. *Bull. Am. Meteorol. Soc.* **99**, 381–402 (2018).
- 59. C. R. Thompson, *et al.*, The NASA Atmospheric Tomography (ATom) Mission: Imaging the Chemistry of the Global Atmosphere. *Bull. Am. Meteorol. Soc.* **103**, 761–790 (2022).
- 675 60. B. B. Stephens, *et al.*, Airborne measurements of oxygen concentration from the surface to the lower stratosphere and pole to pole. *Atmos. Meas. Tech.* **14**, 2543–2574 (2021).
 - 61. G. W. Santoni, *et al.*, Evaluation of the airborne quantum cascade laser spectrometer (QCLS) measurements of the carbon and greenhouse gas suite CO₂, CH₄, N₂O, and CO during the CalNex and HIPPO Campaigns. *Atmos. Meas. Tech.* 7, 1509–1526 (2014).
- 680 62. J. C. Daube, K. A. Boering, A. E. Andrews, S. C. Wofsy, A high-precision fast-response airborne CO₂ analyzer for in situ sampling from the surface to the middle stratosphere. *J. Atmos. Ocean. Technol.* **19**, 1532–1543 (2002).
 - 63. J. D. Bent, "Airborne oxygen measurements over the Southern Ocean as an integrated constraint of seasonal biogeochemical processes," University of California, San Diego. (2014).
 - 64. C. Sweeney, et al., Seasonal climatology of CO2 across north america from aircraft

- measurements in the NOAA/ESRL global greenhouse gas reference network. *J. Geophys. Res.* **120**, 5155–5190 (2015).
- 65. R. Gelaro, *et al.*, The Modern-Era Retrospective Analysis for Research and Applications, 690 Version 2 (MERRA-2). *J. Clim.* **30**, 5419–5454 (2017).
 - 66. S. Kobayashi, *et al.*, The JRA-55 reanalysis: General specifications and basic characteristics. *J. Meteorol. Soc. Japan* **93**, 5–48 (2015).
 - 67. R. F. Keeling, C. D. Keeling, "Atmospheric Flask CO₂ and Isotopic Data Sets Multiple Sampling Stations (Archive 2021-07-01). In Scripps CO₂ Program Data. UC San Diego Library Digital Collections. https://doi.org/10.6075/J0HQ3X30" (2017).

- 68. C. D. Keeling, *et al.*, "Exchanges of atmospheric CO₂ and ¹³CO₂ with the terrestrial biosphere and oceans from 1978 to 2000. I. Global aspects, SIO Reference Series, No. 01-06, Scripps Institution of Oceanography, San Diego, 88 pages" (2001).
- 69. C. Rödenbeck, *et al.*, Interannual sea-air CO₂ flux variability from an observation-driven ocean mixed-layer scheme. *Biogeosciences* **11**, 4599–4613 (2014).

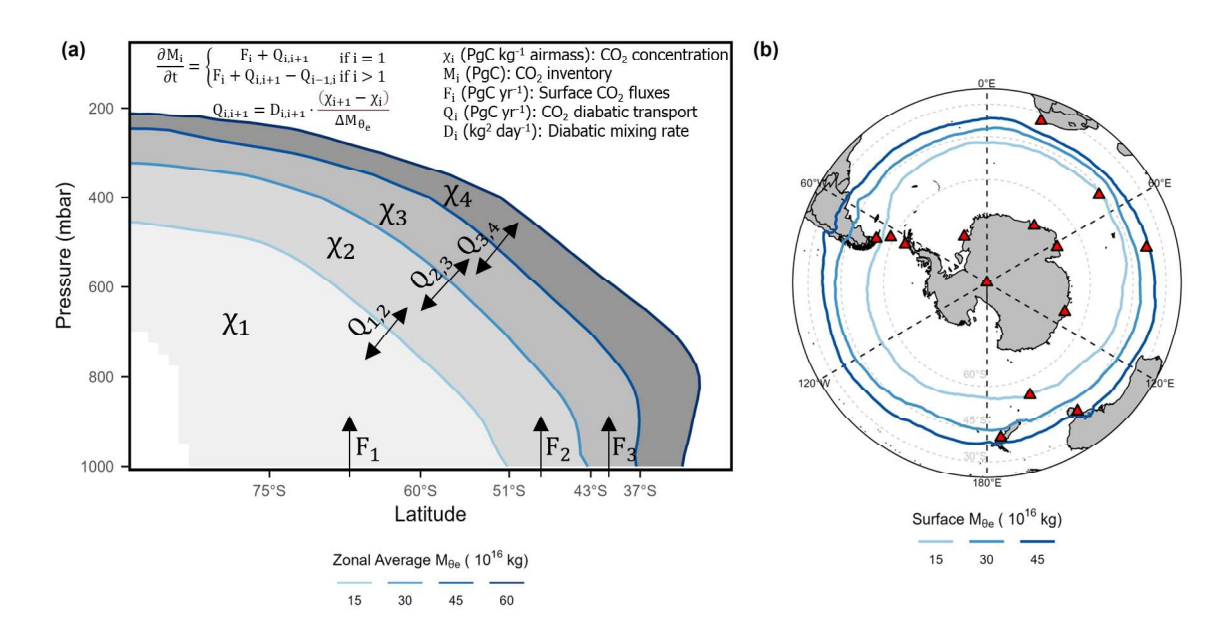


Figure 1: (a) Schematic of the box model. Boundaries of the box model are selected $M_{\theta e}$ surfaces at 15, 30, 45, and 60 $M_{\theta e}$ values (10^{16} kg), which are shown as zonal and 2009-2018 averages. (b) Selected near-surface $M_{\theta e}$ contours as 2009-2018 averages. $M_{\theta e}$ is computed from 3-hourly MERRA-2 reanalysis. These $M_{\theta e}$ bands are nearly fixed with season (*SI Appendix*, Fig. S2). Red triangles show the location of surface stations that are used in the Carbon Tracker 2019b 3-D CO_2 inversion product.

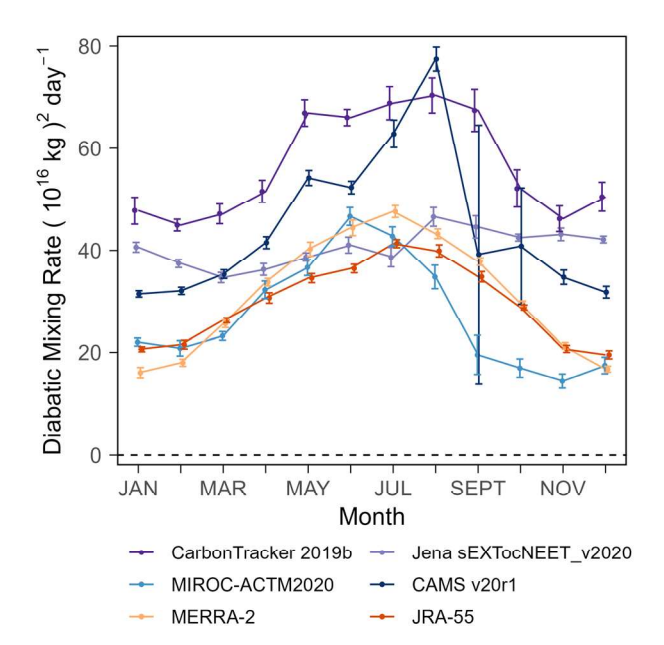


Figure 2: Diabatic mixing rates of the 30 (10^{16} kg) M_{θe} surface. These mixing rates are parameterized from four 3-D CO₂ inversion products and moist static energy budget of two reanalysis products (MERRA-2 and JRA-55). Error bars represent only the interannual variability of parameterized mixing rates, which is shown to be small, with the exception of CAMS in September because of the close-to-zero CO₂ gradient across the 30 (10^{16} kg) M_{θe} surface. Diabatic mixing rates of the 15 and 45 (10^{16} kg) M_{θe} surface are shown in *SI Appendix*, Fig. S3.

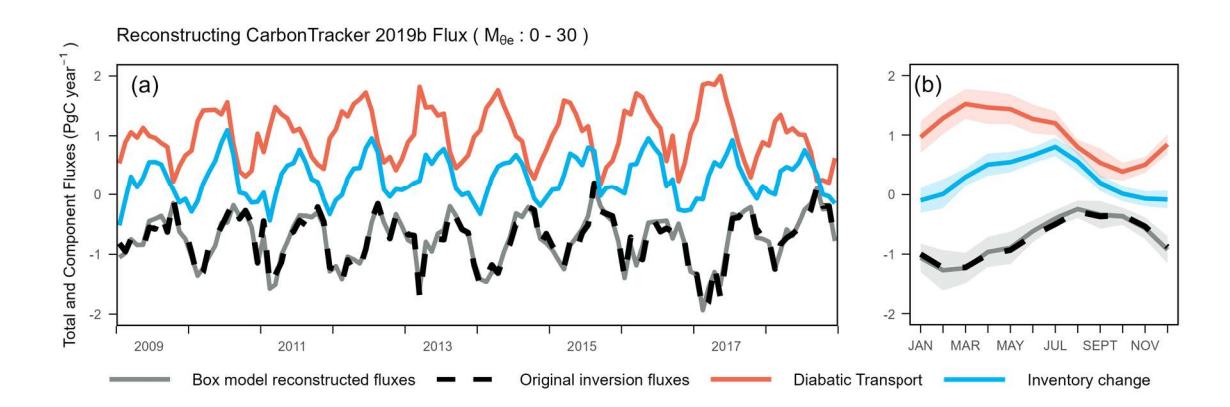


Figure 3: (a) Monthly reconstructed air-sea CO₂ fluxes (solid gray) for the 0-30 (10^{16} kg) M_{θe} band (south of ~ 43°S near the Earth surface) based on CarbonTracker 2019b, compared with the original monthly 3-D inversion fluxes for the same M_{θe} band (dashed black). The other components (i.e., diabatic CO₂ transport and CO₂ inventory change, detailed in Materials and Methods, and Eq. 1) of the box-model reconstruction are shown as well. Positive values of the diabatic transport represent CO₂ transport into the 0-30 M_{θe} band (poleward transport). We note that the inventory change (blue) equals the sum of fluxes (black) and diabatic transport (red). (b) Similar to (a), but showing the flux and other components as climatological monthly averages (2009 to 2018). Shaded regions show interannual variability, which is calculated as the standard deviation over 10 years for the corresponding month. We also show these reconstructions for other 3-D inversion products and other surface M_{θe} bands in *SI Appendix*, Fig. S4-S6.

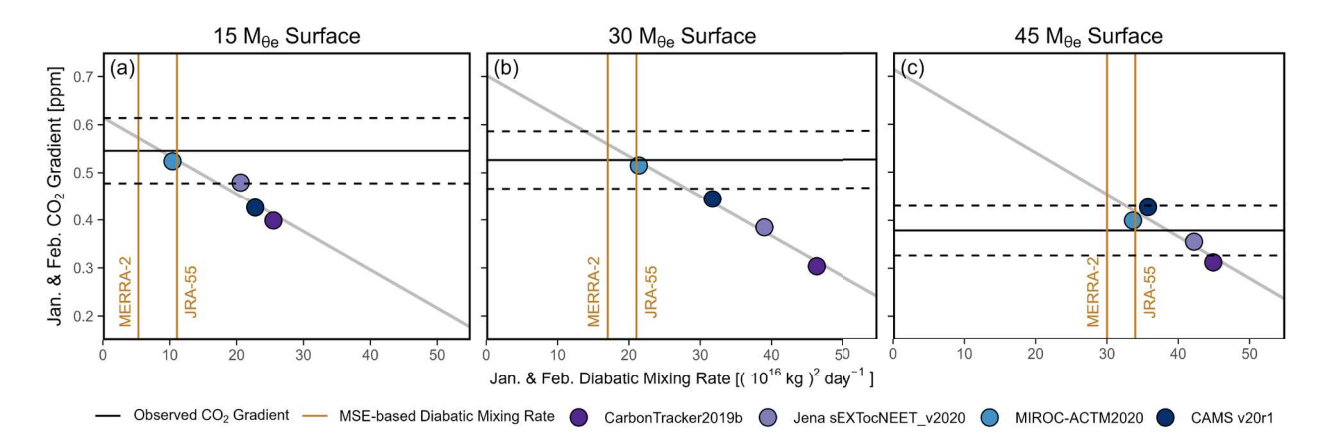


Figure 4: Exploring the correlation between Jan. and Feb. ATM-based mixing rates at each $M_{\theta e}$ surface and simulated atmospheric CO₂ gradients across the corresponding $M_{\theta e}$ surface of four transport models (3-D CO₂ inversion products). Simulated gradients are from 3-D concentration fields averaged at the mean dates of five airborne campaigns or sub-campaigns that took place during January and February (HIPPO1, ATom2, and ORCAS1-3). The corresponding ATM-based mixing rate is calculated as the January and February average. For comparison, we show the observed CO₂ gradients (spatial bias corrected, as detailed in *SI Appendix*, Text S1) as horizontal black lines, which are calculated as the average of the same five campaigns or sub-campaigns, while the dashed lines show the 1 σ uncertainty (measurement and spatial bias correction uncertainty). We also show two MSE-based mixing rates (January and February average) as vertical brown lines. A similar figure exploring the correlation between April to November averaged CO₂ gradient and averaged diabatic mixing rate is presented in *SI Appendix*, Fig. S7.

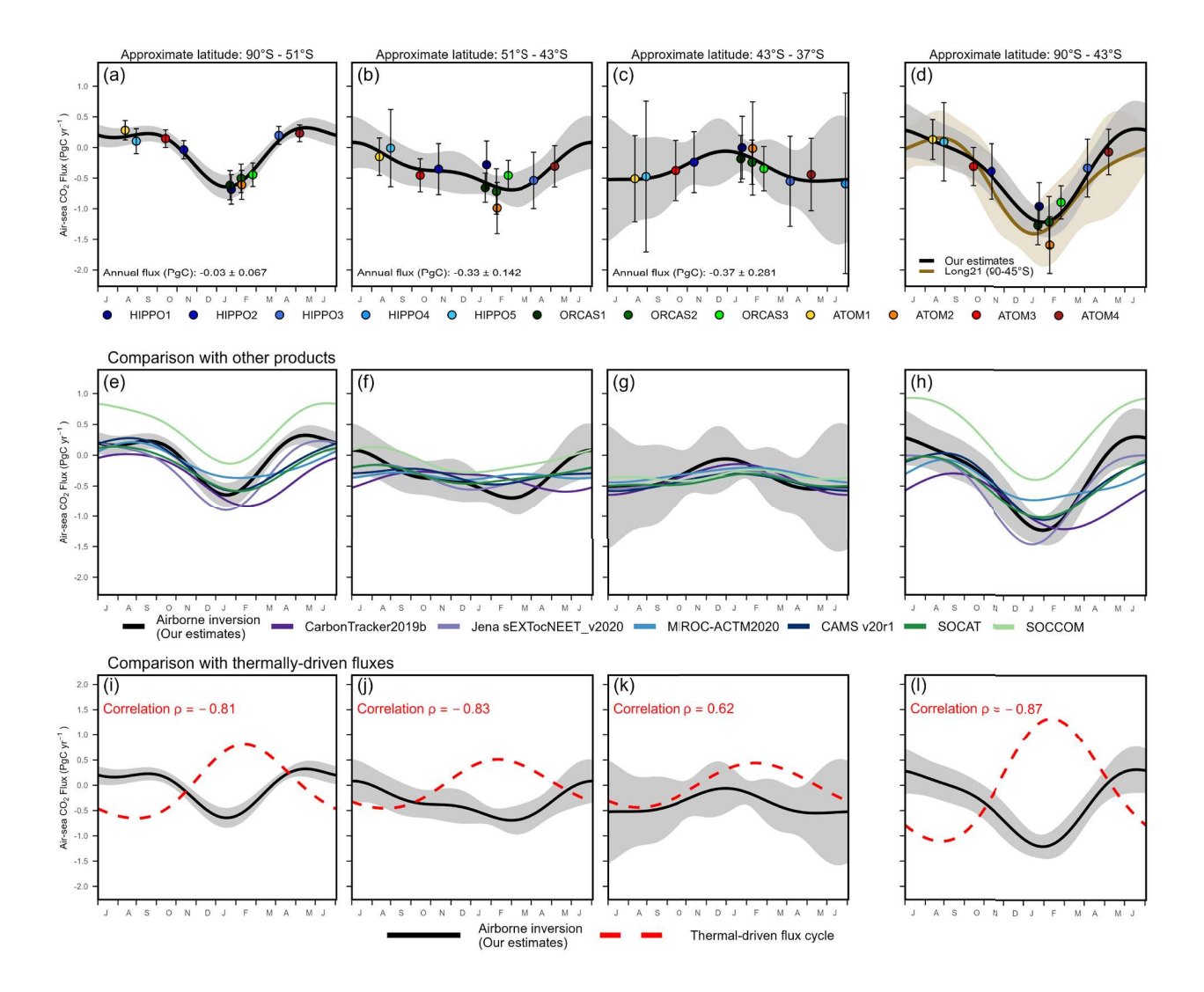


Figure 5: (a)-(d) Seasonal cycle of air-sea CO₂ fluxes (negative as net oceanic uptake) estimated using 4-box model based on airborne CO2 observations and two sets of MSE-based diabatic mixing rates (see Materials and Methods). Each individual point represents the calculated fluxes using airborne observations from the corresponding campaign, centering on the mean date of each campaign, while the black line is a 2-harmonic fit. Error bars represent the 1σ uncertainty of each flux estimate, while shaded regions represent the 1σ uncertainty of the 2-harmonic fits (detailed in SI Appendix, Text S1-2). Values of air-sea CO₂ fluxes calculated for each airborne campaign transect and for each band are summarized in SI Appendix, Table S4. Annual fluxes are from the constant term of the 2-harmonic fitted climatological flux cycles, which is equivalent to integrating the fit over a year. These approximate latitude bands (see top of each panel) are calculated as the zonal average latitude of the corresponding annual average (2009 to 2018) $M_{\theta e}$ surface over the ocean (SI Appendix, Fig. S2). We also show box-model resolved fluxes calculated using the average of 6 sets of mixing rate and each set of mixing rate in SI Appendix, Fig. S10 and S11. In (e)-(h), we compare our estimates with four 3-D CO₂ inversion products, and two neural network interpolated surface ocean pCO₂ products using SOCAT pCO₂ observations alone and SOCCOM pCO₂ observations alone. Details of these products are in SI Appendix, Text S6. The SOCCOM product is a sensitivity run where all shipboard data from SOCAT were excluded (only SOCCOM float data were included). We note that the ocean CO2 flux in Jena sEXTocNEET v2020 is a prior, which is provided by assimilation of surface ocean pCO₂ observations (i.e., not neural-network derived pCO₂) from SOCAT (29) by the Jena mixedlayer scheme (69). The seasonal cycle of each product is calculated as the average between 2009 and 2018, except for SOCCOM, which is averaged from 2015 to 2017. In (i)-(l), we compare our estimates with thermally-driven air-sea CO₂ flux cycles (dashed red, methods in SI Appendix, Text S3), which is derived from assuming 4% pCO₂ increase per degree Celsius increase in seasurface temperature (SST) and using wind-speed dependent gas exchange. We calculate the correlation between the airborne observed flux cycle and the estimated thermal-driven flux cycle of each band. Black solid curves and shaded regions in (e)-(l) are corresponding airborne observed fluxes and 1 σ uncertainty. Panels (i) to (l) have a different y-axis range compared to panels (a) to (h). We also compare our estimates with nine global ocean biogeochemistry models that are used in the Global Carbon Budget 2020 (11, 55) in SI Appendix, Fig. S9.

750

755

760

765

770